Nanoscale Advances

ROYAL SOCIETY OF CHEMISTRY

PAPER

View Article Online
View Journal | View Issue

Cite this: *Nanoscale Adv.*, 2023, **5**, 3655

Development of hierarchical copper sulfide–carbon nanotube (CuS–CNT) composites and utilization of their superior carrier mobility in efficient charge transport towards photodegradation of Rhodamine B under visible light†

Mainak Das,[a] Dhananjoy Das,[a] Sayantan Sil[b] and Partha Pratim Ray *[a]

In this work, the synthesis of visible light sensitive copper sulfide (CuS) nanoparticles and their composites with carbon nanotubes (T-CuS) *via* a solvothermal technique is reported. The synthesized nanoparticles (NPs) and their composites were significantly characterized by powder X-ray diffraction (PXRD), scanning electron microscopy, transmission electron microscopy, X-ray photoelectron spectroscopy, UV-vis spectroscopy, photoluminescence (PL) spectroscopy and thermogravimetric analysis (TGA). The effect of carbon nanotubes (CNTs) on the crystallinity, microstructures, photo-absorption, photo-excitation, thermal stability and surface area of CuS was investigated. The current–voltage (*I vs. V*) characteristics of both CuS and T-CuS based Schottky diodes were measured to determine the charge transport parameters like photosensitivity, conductivity, mobility of charge carriers, and transit time. The photocatalytic performance of bare CuS and T-CuS in the decomposition of Rhodamine B dye was studied using a solar simulator. The T-CuS composite showed higher photocatalytic activity (94%) compared to bare CuS (58%). The significance of charge carrier mobility in transferring photo-induced charges (holes and electrons) through complex networks of composites and facilitating the photodegradation process is explained. Finally, the reactive species responsible for the Rhodamine B degradation were also identified.

Received 29th March 2023
Accepted 30th May 2023

DOI: 10.1039/d3na00204g

rsc.li/nanoscale-advances

Introduction

Organic dyes and pigments discharged into water sources, mostly by the paint and textile industries, are causing serious environmental issues and harming the ecosystem in other ways.[1] Over the last few decades, various biological and physicochemical experiments based on physical as well as chemical adsorption approaches have been conducted to decompose these industrial pollutants. However, these processes often produce secondary pollutants and are not cost-effective from the economic viewpoint.[2] The photocatalytic approach based on semiconductor materials has demonstrated significant efficiency in wastewater purification among all advanced oxidation techniques known to exist.[3] There are some well-known semiconducting photocatalysts, namely TiO_2 and ZnO, which have been widely used to decompose organic pollutants, but their use is hindered due to their wide range bandgaps, which are 3.2 eV and 3.37 eV for TiO_2 and ZnO, respectively, limiting their light absorption mainly in the ultraviolet (UV) region of the solar spectrum.[4,5] This reduces the redox reactions with the impurities and significantly affects the rate of degradation.[6]

On the other hand, copper(II) sulfide (CuS) has a narrow direct bandgap of 2.29 eV, due to which it can efficiently capture visible light from the solar spectrum, making it practically function as a 'visible-light-driven photocatalyst'. It also has excellent optical and electronic properties which show great potential in many fields like solar cells,[7] energy storage,[8] gas sensors,[9] biosensors[10] and photocatalysis.[11] Copper sulfide has some excellent features, such as its environmentally friendly and non-toxic nature, low cost, biocompatibility, higher physical and chemical stability and ease of recyclability which

[a]*Department of Physics, Jadavpur University, Kolkata 700032, India. E-mail: parthapray@yahoo.com*

[b]*Department of Physics, University of Engineering and Management, University Area, Action Area III, B/5, Newtown, Kolkata 700160, India*

† Electronic supplementary information (ESI) available: Device fabrication method, calculation of bandgap and dielectric constant, weight (%) test of CNT, charge transfer characteristics of CNT, adsorption of RhB by the catalysts, photodegradation process, function of H_2O_2 in the degradation process, optimization of the composite material with different CNT content, identification of reactive species, recycling test, photocatalytic activity of a non-azo dye, Fig. S1–S9, and eqn (S1) and (S2). See DOI: https://doi.org/10.1039/d3na00204g

enhances its effectiveness as a prospective photocatalyst. On the other hand, CuS nanomaterials also have an intrinsic drawback of having poor photocatalytic performance, especially when exposed to visible light, due to the quick electron (e^-)–hole (h^+) recombination. There have been several attempts to enhance the electron transfer during the photocatalytic process by reducing the electron–hole recombination in these materials. Carbon nanomaterials are eco-friendly, cost-effective and good electron acceptors, so they can suppress electron–hole recombination effectively.[12] Among them, carbon nanotubes (CNT) are unique in terms of their morphological, structural, and electrical characteristics, such as their organised structure with a high surface to volume ratio, light weight, and high electrical conductivity. CNT increases the migration rate of photogenerated electrons, thereby pushing electrons and holes away which prohibits electron (e^-)–hole (h^+) recombination. Absorption of light also induces electrons into the CNTs and enhances the participation of electrons in the photocatalytic reaction.[13,14] For higher photocatalytic performances, the electrons are expected to swiftly transfer and their subsequent recombination should be as slow as possible.[15] Further, the fast electron transfer depends on the mobility of the carriers. To enhance the mobility and the associated charge carrier transport properties, CNT is incorporated with bare CuS in this work. This enhanced mobility of the charge carriers in the T-CuS composite reflects in better photocatalytic performances than for bare CuS. This report describes the synthesis of a carbon nanotubes–copper sulfide (T-CuS) composite and demonstrates its capability to decompose the organic dye Rhodamine B in the presence of visible light.

Experimental

Materials

The chemicals used in this study were copper(II) nitrate trihydrate ($Cu(NO_3)_2 \cdot 3H_2O$), ethylene glycol ($HOCH_2CH_2OH$), deionized (DI) water, absolute ethanol (C_2H_6O) and hydrogen peroxide (H_2O_2). All of them were purchased from Merck (Merck Specialities Private Limited). In addition, sodium sulphide ($Na_2S \cdot 9H_2O$) and multi-walled carbon nanotubes (CNT) were purchased from RANKEM Laboratory Reagent and from Sigma Aldrich, respectively. All the chemicals in the synthesis were used without any additional purification.

Synthesis of CuS nanoparticles

Here, a solvothermal method was used to synthesise the CuS nanoparticles (NPs). At first, 0.9964 g of $Cu(NO_3)_2 \cdot 3H_2O$ was mixed with 30 mL ethylene glycol and placed on a magnetic stirrer for 30 min to prepare a homogeneous solution (solution 1). Then, 0.9604 g of $Na_2S \cdot 9H_2O$ was mixed with 20 mL ethylene glycol and another homogeneous solution was prepared *via* magnetic stirring for 30 min (solution 2). Thereafter, solution 2 was put into solution 1 drop by drop and the collected mixture was stirred for 1 h. Next, the obtained solution was transferred to a Teflon-lined solvothermal autoclave which was kept inside an oven at a temperature of 160 °C for 16 h. After that the precipitate was rinsed with DI water (four times) and ethanol (four times) and finally collected by centrifugation techniques. At the end, the final product, CuS nanoparticles, was collected and dried at 60 °C for 16 h.

Synthesis of the CNT–CuS composite

Here, a similar solvothermal method was used to synthesise the CNT–CuS composites (T-CuS). In this process, a certain amount (3%) of carbon nanotubes (CNTs) was dispersed in $Cu(NO_3)_2$ precursor solution and then stirred for 30 min. After that, Na_2S solution was dropwise added into the previous mixer. This final prepared solution was kept under magnetic stirring for 6 h. Then, the final solution was transferred to a Teflon-lined autoclave. After that, the autoclave was placed in a hot air oven at a temperature of 160 °C for 16 h. Finally, the collected samples were washed multiple times with DI water and absolute ethanol and then kept on a hot plate at 60 °C for 12 h. The synthesis process of the CNT–CuS composite is shown in Fig. 1.

Material characterization techniques

The crystallographic structure and phase purity of the synthesized materials (CuS and T-CuS) were analysed using a powder X-ray diffractometer (Bruker D8 Advance) having Cu-K_α (λ = 1.5418 Å) radiation, operated at a scan rate of 0.02° s^{-1}. The surface morphology was studied with the help of a scanning electron microscope (FEI Inspect F50) and the elemental combination was determined using an EDX (energy dispersive X-ray) analyser. Information regarding the microstructure of the synthesised materials was analysed with the help of a transmission electron microscope (JEOL JEM 2100 F). XPS (X-ray Photoelectron Spectroscopy; Omicron Nanotechnology) with Al-K_α radiation (E = 1486.7 eV) was utilised to examine the electronic states of the elements present on the surface of the samples. The absorption spectra and the photocatalytic behaviour of the synthesized materials were recorded using a UV-vis (PerkinElmer, Lambda 365) spectrophotometer and a solar simulator [Model 10500, Abet Technologies], respectively. The photoluminescence (PL) spectra were collected using a spectrofluorimeter (Cary Eclipse fluorescence spectrometer, Agilent Technologies). The thermal stability of both of the materials was investigated using a thermogravimetric analyser (DTG-60H, Shimadzu) within the temperature range from 30 °C to 800 °C in a N_2 atmosphere. The estimation of the Brunauer–Emmett–Teller (BET) surface area of the synthesised materials by N_2 adsorption–desorption was done using an Autosorb iQ2

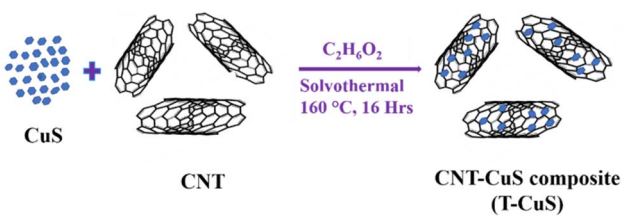

Fig. 1 Schematic diagram of the synthesis process of the CNT–CuS nanocomposite.

(Quantachrome, USA) at 77 K. The measurements of current–voltage (*I–V*) characteristics were performed with a source measurement unit (Keithley 2635B).

Results and discussion

Structural properties

XRD analysis. Fig. 2 displays the PXRD patterns of CuS and the T-CuS nanocomposites. The diffraction peaks of the prepared CuS observed at $2\theta \approx 27.12°$, 27.68°, 29.28°, 31.78°, 32.85°, 38.83°, 47.94°, 52.71°, 59.34°, 73.99° and 79.07° were assigned to the (100), (101), (102), (103), (006), (105), (110), (108), (116), (208) and (213) crystallographic planes of the hexagonal copper sulfide structure (JCPDS Card No. 06-00464, $a = 6.792$ Å and $c = 16.34$ Å). The narrow, sharp peaks indicate the crystallinity of the bare CuS. The peaks at 25.89° and 43.56° were assigned to the (002) and (101) planes of the CNTs respectively.[16] This XRD pattern showed that the major diffraction peaks of the T-CuS composite were similar to those of bare CuS, which explains that the attachment of CNT did not affect the preferred orientations of CuS or result in the growth of a new crystallographic phase. Also, very small diffraction peaks of CNT were observed in the composite. This might have occurred due to the low amount of loading and relatively weak diffraction peaks of CNT.[17]

FESEM analysis. The FESEM images of the synthesized CuS and T-CuS nanocomposite are displayed in Fig. 3. The microstructural and morphological information from SEM images suggests that the CuS and T-CuS composite consist of nearly hexagonal-shaped nanostructures, which contain some agglomeration. It is clear in Fig. 3b that CuS nanoparticles were properly attached to the CNT during the solvothermal synthesis. From the EDAX spectrum (Fig. 3c), the appearance of constituent elements (C, O, Cu and S) in the composite was precisely noted. Further, the quantitative interpretation of the EDAX exhibited that in the synthesized material, the molar ratio of Cu to S was close to one, indicating the stoichiometric formation of CuS NPs.

TEM analysis. The TEM images (Fig. 4a and b) further revealed that the hexagonal-like CuS NPs were uniformly attached to the carbon nanotubes, suggesting the formation of a strong interface with nominal aggregation of particles. The finer attachment between the CuS NPs and CNT (Fig. 4b) by this familiar bonding could assist the transfer of charge carriers, and thus, suppress e^-–h^+ recombination – which is advantageous for better photocatalytic response which will be discussed in the following paragraph. Fig. 4d shows the SAED pattern of T-CuS NPs with various concentric diffraction rings, suggesting the polycrystalline nature of the materials.

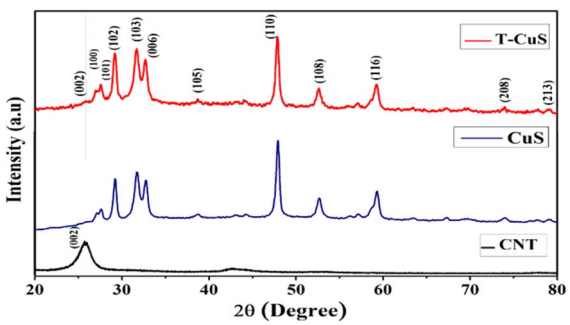

Fig. 2 XRD patterns of the synthesized CuS and T-CuS nanocomposite.

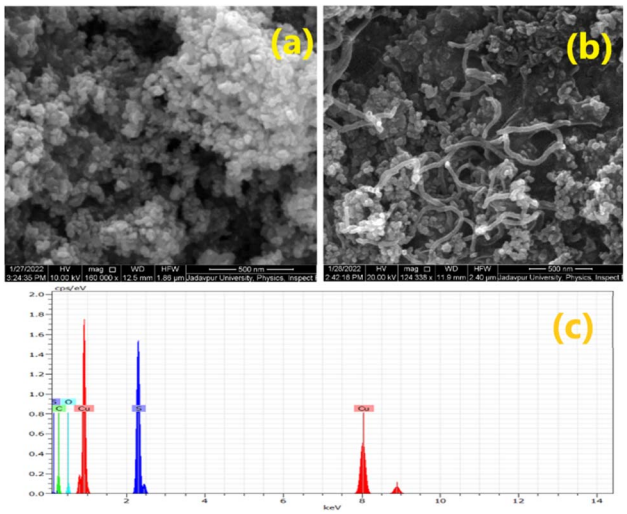

Fig. 3 FE-SEM images of (a) CuS and (b) T-CuS, and (c) EDAX spectrum of the T-CuS nanocomposite.

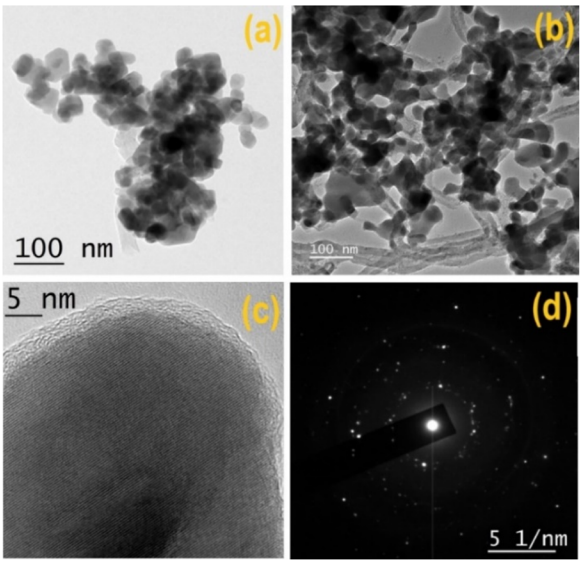

Fig. 4 TEM images of (a) CuS and (b) the T-CuS composite. (c) HRTEM and (d) the SAED pattern of CuS NPs attached to CNT.

XPS study. X-ray photoelectron spectroscopy (XPS) of T-CuS nanostructures was carried out to examine the elemental composition and identify the chemical bond type as well as the oxidation states. The existence of the C, Cu, S, and O in the T-CuS composite was verified by the XPS survey spectrum scan (0–1200 eV) (Fig. 5a), confirming the presence of elemental Cu and S in the nanocomposite. The core level XPS spectra of C 1s,

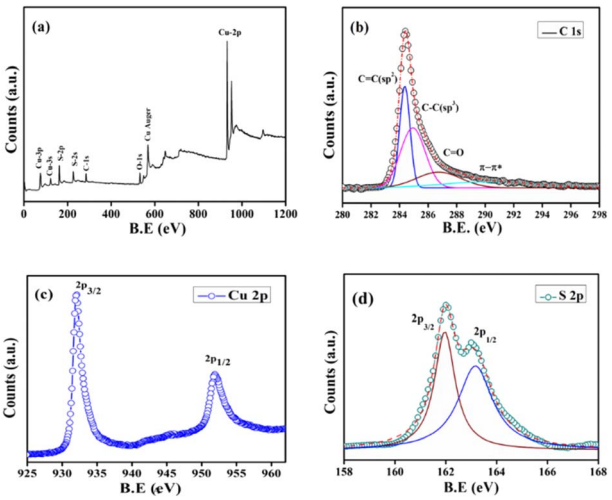

Fig. 5 XPS analysis: (a) full scan spectrum of T-CuS; (b) C 1s spectrum for the T-CuS composite; narrow scan of (c) Cu 2p and (d) S 2p states.

Cu 2p and S 2p are shown in Fig. 5b–d, respectively. The XPS peak for C 1s of the composite was deconvoluted into four distinct peaks centred at the corresponding binding energies (B.E.) of 284.40, 285.10, 287.60 and 290 eV, which could be ascribed to C=C, C–C, C=O and π–π* shake-up features respectively (Fig. 5b).[18] This suggests the probable existence of graphitic layers which prefer fast electron transfer and the O_2-containing group establishes strong interaction in between the aqueous solution and the nanocomposite at the time of photocatalytic decomposition, which will be discussed in the following. The higher resolution XPS of Cu 2p which is shown in Fig. 5c displays two distinct peaks at 932.4 eV and 952.3 eV. The difference between these states is 19.9 eV, which is consistent with the previously reported data for Cu $2p_{3/2}$ and Cu $2p_{1/2}$ states.[19] These peaks can be assigned to the Cu^{2+} state in CuS nanostructures. The higher resolution XPS spectrum of S 2p (Fig. 5d) indicates the existence of two peaks at B.E. values of 161.9 eV and 163.3 eV, which could be attributed to S $2p_{3/2}$ and S $2p_{1/2}$ states, respectively.[20] S^{2-} species are responsible for the detection of these two peaks.

Optical properties

UV-vis absorbance study. UV-vis absorbance spectra of the synthesized CuS and T-CuS nano-composite were recorded in the 300–750 nm wavelength range (Fig. 6a) to study their optical properties. The optical band gaps (E_g) of the catalysts were deduced followed by Tauc's equation eqn (S1).†[21] The estimated value of the bandgaps of the synthesised CuS and T-CuS from Tauc's plot (Fig. 6b) was 2.29 eV and 2.19 eV respectively, close to the previously reported value.[22] The broadness of the absorption band and the reduced bandgap of the CNT-attached material compared to bare NPs suggests the improvement in photon absorption and more e^-–h^+ pair generation for the photocatalytic experiment. The more generated e^-–h^+ pairs participating in the degradation process should enhance the deterioration rate for T-CuS than bare CuS.

Photoluminescence (PL) study. PL was used to study the interaction among the holes and electrons, originating from the excitation of photons in the synthesized catalysts. Fig. 7 shows the PL spectra of CuS and the T-CuS composite at 370 nm excitation. The bare CuS exhibits an eminent emission centred at 425 nm, which was sufficiently weakened after loading CNT.[23,24] This is because there exists an effective interfacial linkage in the composite materials, so electrons and holes acquire a dedicated pathway to interact between CuS and CNT layers. The high electrical conductivity and sp^2 hybridization of carbon atoms show high mobility of photo-induced holes and electrons. The electrons could easily transfer from the excited CuS to the carbon nanotube through the π-conjugated carbon network and the 'quenching' of fluorescence occurs. The CuS–CNT composites are efficient at suppressing the recombination rate of electrons and holes by fast electron transfer. This kind of extended separation of photo-induced charge carriers and their immediate processes is advantageous for catalytic degradation, which will be discussed in the following.[24,25]

Thermal stability analysis. Thermal stability of the as-synthesized CuS and T-CuS composite was examined by thermogravimetric analysis (TGA), executed with a gradual increase in temperature (10 °C min^{-1}) ranging from 25 °C to 800 °C in a N_2 atmosphere. Fig. 8 shows the TGA graph of the T-CuS composite, showing two definite stages of weight loss where 78% of weight remained up to 800 °C temperature. The initial weight loss (7.35%) for bare CuS was observed between 100 and 300 °C which indicates solvent desorption and moisture

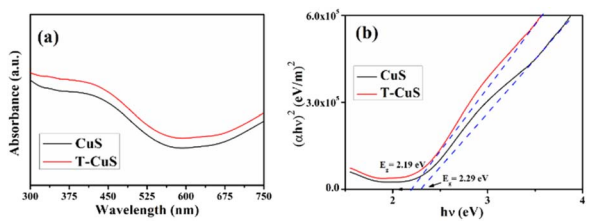

Fig. 6 (a) Absorption (optical) graph of bare CuS and the T-CuS composite. (b) Tauc's plot to obtain the band gap of CuS and T-CuS.

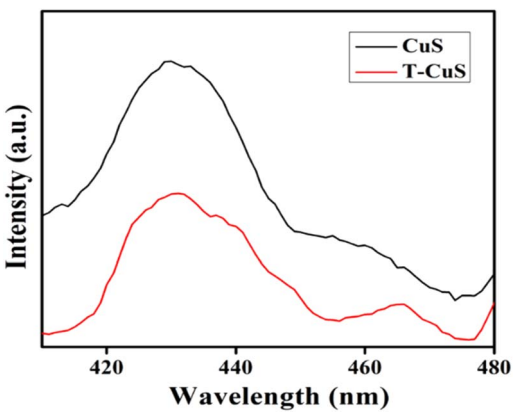

Fig. 7 Photoluminescence spectra of CuS and the T-CuS nanocomposite.

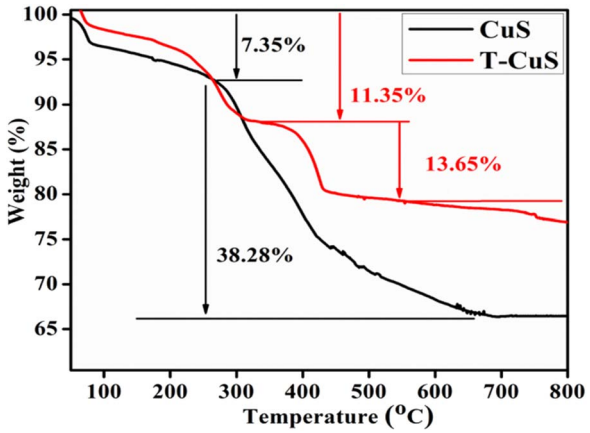

Fig. 8 TGA curves of bare CuS and the T-CuS composite.

absorption. Additionally, the bare CuS underwent a rapid weight loss (38.28%) at around 300–650 °C due to the decomposition of CuS into Cu_2S and phase transition of sulfur element, leaving 67% residue.[26] The first weight loss (11.35%) of T-CuS at around 100–300 °C is observed due to removal of solvent and the residual organic molecules adsorbed on the samples. In the second stage (300–450 °C), the weight loss (13.65%) for T-CuS was observed due to the oxidation of CNT and phase conversion of CuS. This result indicates that the CNT composite (T-CuS) is thermally more stable than bare CuS.

BET surface area analysis. N_2 adsorption/desorption isotherms (Fig. 9) were also recorded at 77 K to gain more information about the Brunauer–Emmett–Teller (BET) specific surface area of the bare CuS and T-CuS nano-composite.[27] According to the BET analysis, the bare CuS and T-CuS composite displayed specific surface areas of 50.67 $m^2\ g^{-1}$ and 86.83 $m^2\ g^{-1}$, respectively, showing that the CNT-based composite had a greater surface area as expected.[28] The rate of photo-absorption and effective molecular diffusion will increase with a larger surface area. Generally, a greater absorbance cross-section is preferred in photocatalytic processes, and it is expected that the CNT-based composite will meet these requirements as shown later. The larger surface area of CNT provides adequate interfacial contact with CuS nanoparticles which suppresses the recombination of e^-–h^+ pairs and enhances the charge transport properties for T-CuS compared to CuS.

Electrical properties. To understand the electronic charge transfer characteristics of the above-discussed materials, current–voltage (*I–V*) measurements of the Schottky diodes fabricated as (Al/CuS/ITO) & (Al/T-CuS/ITO) structures (ESI†) were made using a bias voltage range of ±1 volt under dark and light (~1000 W m^{-2}) conditions at 300 K temperature. The measurement of charge flow, known as dc conductivity (σ), was evaluated from the ohmic (linear) region of the characteristic curves (Fig. 10a) of both devices under dark and illumination/light conditions (Table 1). A notable increment in current under illumination conditions reflects the photosensitivity of the synthesized materials. The definition of photosensitivity (S) (eqn (1)), $S = I_v/I_d$ (here, $I_v = I_l - I_d$ is denoted as light-induced current; on the other hand, I_d denotes the current under dark conditions), was derived for two different devices.[29] The CNT-based device with greater absorption capacity has better sensitivity than bare CuS (Table 1). In addition, the higher conductivity of the composite material means efficient charge transport with excellent mobility. For any semiconductor material, carrier mobility determines how fast a carrier, *i.e.*, e^- or h^+, can move through its complex network and reach active sites before recombination. Since CNT provides higher electronic mobility (~10^5 $cm^2\ V^{-1}\ s^{-1}$ at 300 K), the enhancement of electron transport and e^-–h^+ pair separation through its high-quality complex network is expected.[30]

To observe the overall effect of CNT in the photo-degradation process and to better understand the charge transfer mechanism, the current–voltage (*I–V*) mechanism was further analyzed by introducing transit time (τ) and carrier mobility (μ_{eff}). For this purpose, log *I vs.* log *V* graphs are plotted for the positive voltages as shown in Fig. 10b, which shows two distinct linear regions, suggesting different conduction mechanisms. Interfacial trap states at the metal–semiconductor junction modify the conduction mechanism of charge carriers which revised the *I–V* characteristics. In small bias (region I), current shows ohmic ($I \propto V$) behaviour with a slope value of approximately one. At this region, the current is guided by the intrinsic charge carriers of the material.[31] The carriers injected from the junction spread over the space at the intermediate potential difference (region II) and create a spatially distributed field of charge. This field dominates the charge carriers and their "mobility" becomes a key factor for the quadratic current ($I \propto V^2$).[32,33] Furthermore, space charge limited current (SCLC)

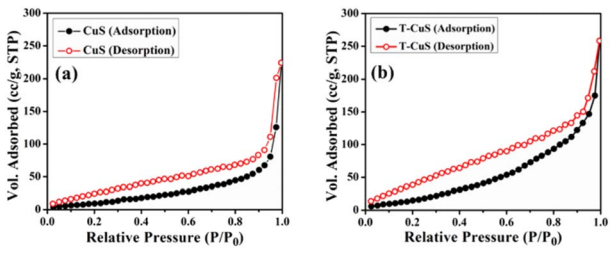

Fig. 9 N_2 adsorption/desorption isotherms of (a) CuS and (b) the T-CuS composites.

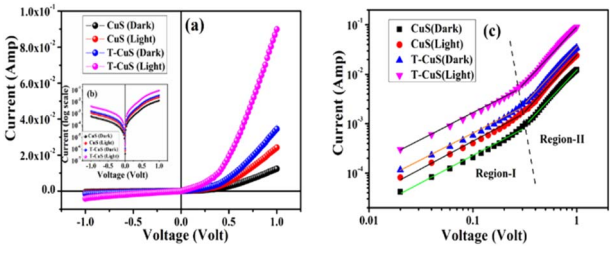

Fig. 10 (a) Current–voltage (*I–V*) plots, (b) log scale *I vs. V* curves and (c) log *I*–log *V* plot of the bare CuS and T-CuS composite-based Schottky diodes under dark and illumination conditions.

Table 1 Charge transport parameters

Sample	Photosensitivity (S)	Conditions					
		Dark conditions	Light conditions	Dark conditions	Light conditions	Dark conditions	Light conditions
		Conductivity (σ) (S m^{-1})		Mobility (μ_{eff}) (m^2 V^{-1} s^{-1})		Transition time (τ) (s)	
CuS	1.01	3.42×10^{-4}	6.71×10^{-4}	2.32×10^{-5}	5.39×10^{-5}	1.54×10^{-8}	8.32×10^{-9}
T-CuS	2.05	9.57×10^{-4}	2.48×10^{-3}	7.98×10^{-5}	2.67×10^{-4}	7.92×10^{-9}	3.20×10^{-9}

theory was used in this region to determine the effective carrier mobility (μ_{eff}) and carrier transit time (τ).

The electron mobility was evaluated from the slope of the I–V^2 plot (Fig. 11a and b), using the equation of Mott–Gurney,[33]

$$I = \frac{9\mu_{eff}\varepsilon_0\varepsilon_r A_{eff}}{8}\left(\frac{V^2}{d^3}\right) \quad (1)$$

where A_{eff}, ε_0, ε_r and d represent the effective area of the diode, the permittivity of free space, the dielectric constant of the material (Fig. S2 and eqn (S2) in the ESI†) and the thickness of the diode, respectively. The carrier transit time or transition time (τ) was also extracted using the following equation,[34]

$$\tau = \frac{9\varepsilon_0\varepsilon_r A_{eff}}{8d}\left(\frac{V}{I}\right) \quad (2)$$

The calculated values of μ_{eff} and t are given below in Table 1. Our results reflected higher mobility for the carbon nanotube and its effective contribution to the transfer of charge carriers smoothly. The CNT-based composite showed greater mobility & transit time than the bare CuS NPs. The result shows compatibility with previously reported data of a carbon-based (rGO) composite.[35,36] Both under dark and illumination conditions, the mobility of carriers increased remarkably up to 4–5 times. The enrichment of mobility & transition time can increase the efficiency of charge transfer and thus the photocatalytic activity.

Transient photo-response measurements and electrochemical impedance spectroscopy (EIS) were performed to investigate the photo-electrochemical characteristics of the as-prepared catalysts, and the results are shown in Fig. 12a and b respectively. The photocurrent intensity of the T-CuS composite was found to be significantly higher (Fig. 12a) than that of the bare CuS, as expected. This result suggests that incorporating CNT into the CuS nanoparticles could facilitate the separation of photo-generated electrons and holes and their swift transfer through the complex network. Furthermore, the EIS Nyquist spectra, which constitute an effective tool for investigating the conductance and charge transfer properties, revealed that the diameter of the semi-circular arc for the T-CuS composite was significantly smaller than for the bare CuS (Fig. 12b). This finding confirms that the addition of CNT significantly reduced the charge transfer resistance in the composite material, allowing electrons and holes to migrate to active sites during the degradation process, as discussed further below.

Photocatalytic activity. Photocatalytic decomposition of RhB under a solar simulator is used to investigate the photocatalytic behaviour of bare CuS and the T-CuS nanocomposites. The

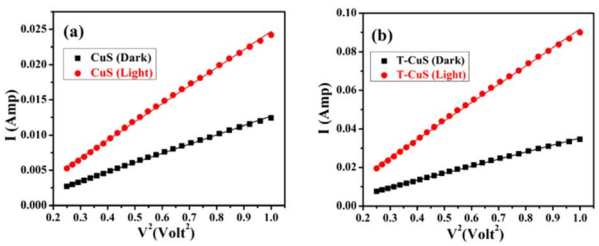

Fig. 11 The I *vs.* V^2 plot for the SCLC region of (a) CuS and (b) the T-CuS nanocomposite.

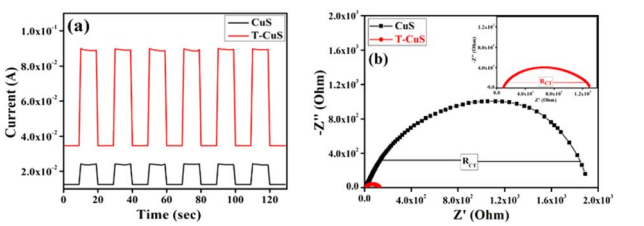

Fig. 12 (a) Transient photocurrent response and (b) EIS Nyquist plots of CuS and the T-CuS composite.

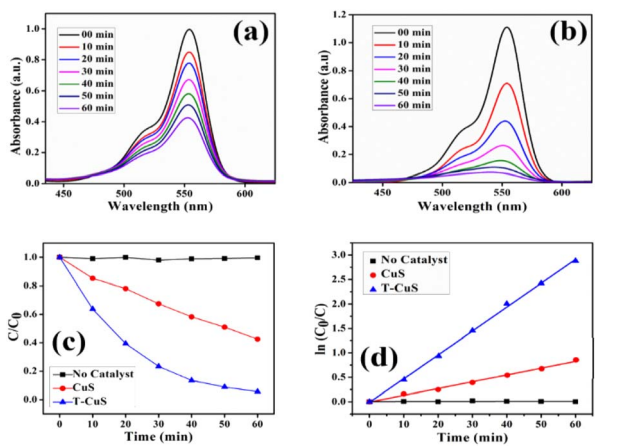

Fig. 13 Absorbance spectra of aqueous RhB solution at different intervals of time in the presence of (a) CuS and (b) the T-CuS nanocomposite under solar irradiation. (c) Photocatalytic degradation behaviour of RhB solution. (d) ln(C_0/C) *vs.* time plot for RhB solution in the presence of CuS and T-CuS catalysts.

degradation procedure was recorded by monitoring the major absorption peaks of aqueous RhB solution centred at 553.5 nm using a UV-vis spectrometer (Fig. 13a and b) and the decomposition process was determined using the following equation

$$\text{Degradation } (\%) = \frac{C_0 - C_t}{C_0} \times 100 \quad (3)$$

where C_0 and C_t represent the RhB concentration at time $t = 0$ & t = time after its initial condition, respectively.[37] The linear behaviour of the $\ln(C_0/C)$ *vs.* exposure time (min) graph of both bare CuS and the T-CuS composites (Fig. 13d) indicates the presence of pseudo-first-order decomposition kinetics.[38] No significant change in RhB concentration was observed in the catalyst-free suspension after exposure to solar-simulated light for 60 minutes. It was found that the addition of the bare CuS catalyst bleached the RhB solution to 58% of its initial concentration. Furthermore, the T-CuS nanocomposites enhanced the degradation by up to 94% due to the synergistic effect of CuS-NPs and CNTs (Fig. 13c). The recycling test in Fig. S8 (ESI†) demonstrated that the decomposition efficiency of the T-CuS catalyst did not change significantly after repeated use for three cycles.

The reactive species trapping experiments were carried out to determine the active species in the 3% T-CuS photocatalytic system. First, 0.1 mmol of methyl alcohol (MeOH), a scavenger of photogenerated h^+, 0.1 mmol of isopropyl alcohol (IPA), a scavenger of hydroxyl $^{\bullet}OH$, and 0.1 mmol of benzoquinone (BQ), a scavenger of superoxide $^{\bullet}O^{2-}$ (ref. 39), were separately added in the photodegradation system. Further, the photodegradation experiment was performed under the same procedure without adding scavengers. The absorption plots of degraded RhB by T-CuS in the presence of different scavengers are shown in Fig. S7 (ESI†). Fig. 14 shows the effect of the scavengers on the degradation percentage of RhB with 60 min irradiation time.

As seen in Fig. 14, the RhB solution degraded up to 86% of its initial concentration which demonstrates that the decomposition of RhB was slightly suppressed in the presence of IPA, as compared to 94% in the absence of scavengers. This finding indicates that $^{\bullet}OH$ has a minor impact on the degradation of RhB using the T-CuS catalyst. In case of MeOH, the value of (C/C_0) was not reduced below 42%, indicating that holes (h^+) play a significant role in RhB degradation. However, when BQ was present during the reaction, the concentration of (C/C_0) was somewhat reduced by up to 68%. This suggests that the $^{\bullet}O^{2-}$ radical is also markedly responsible for photocatalytic degradation of RhB. Here, RhB degradation was observed to be obviously inhibited on the addition of BQ and MeOH; in contrast, IPA had a very small effect on the dye degradation. This implies that the photogenerated holes (h^+) and $^{\bullet}O^{2-}$ radicals play the main role in the removal process of the dye, whereas $^{\bullet}OH$ plays a minor role in the dye degradation.

To explain the synergistic effect of CNTs and CuS in the composite, we analysed the photocatalytic degradation process. In the presence of visible light illumination, excitons of interfaces are generated on the surface of CuS NPs and segregated into free holes in the valence band (VB) & free electrons in the conduction band (CB). However, the photogenerated h^+ and e^- tended to recombine before the appearance of the active site resulting in a poor photocatalytic response. When the CuS NPs bind with CNTs, the photo-induced e^- in the conduction band of CuS can be separated effectively at the carbon nanotube interfaces, leaving h^+ in the valence band of CuS due to its favourable energy level (Fig. 15).[40,41] CNT is photoexcited to produce electrons in its lowest unoccupied molecular orbital (LUMO) and holes in its highest occupied molecular orbital (HOMO). It is well known that CNT is an excellent electron acceptor, which will trap the CB electrons of CuS. Simultaneously, the photoexcited CNT is a good electron donor, readily leading to the migration of the photoexcited electrons in the LUMO of CNT to the CB of CuS. The interesting electron transfer process can efficiently prevent the recombination of the CB electrons with the VB holes in CuS. This is the dominant mechanism resulting in the enhanced photodegradation performance of the T-CuS composites compared to bare CuS.[42] Therefore, photo-generated electrons in CuS can effortlessly reach the active site through the CNT network and reduce the dissolved O_2 present in the aqueous medium into the highly reactive superoxide anion (O^{2-}) and react further with H_2O to form hydroxyl (OH*) radicals.[43] Furthermore, photo-induced h^+

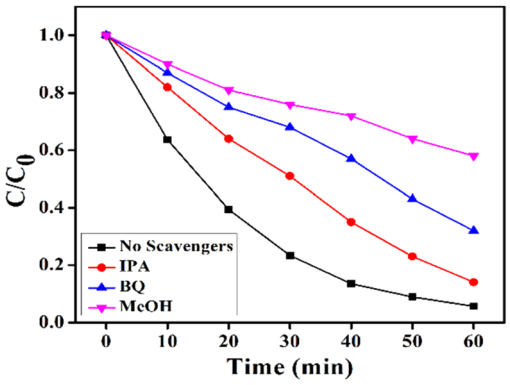

Fig. 14 Photocatalytic degradation of RhB aqueous solution by T-CuS in the presence of IPA, BQ, MeOH and no scavengers.

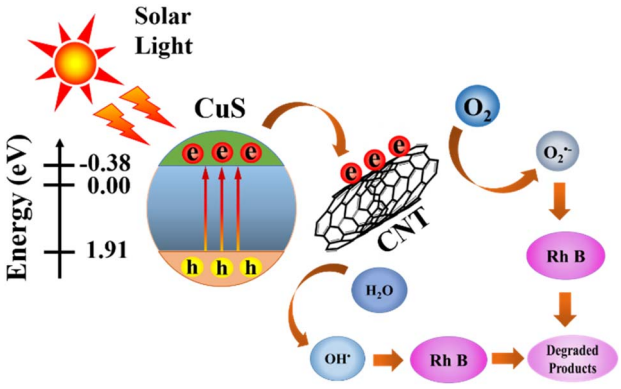

Fig. 15 Pictorial representation of photocatalytic degradation of RhB in the presence of the T-CuS nanocatalyst under a solar simulator.

can react also with H_2O or OH^- to oxidize them to $OH^{\bullet}$.[44] The $O^{2\bullet-}$, $OH^{\bullet}$ and the photo-generated h^+ are jointly involved in the decomposition process of RhB solutions.[45,46] Fig. 15 shows a pictorial representation of the photocatalytic activity of the T-CuS photocatalyst.

Conclusion

CuS NPs were synthesized successfully and the CNT incorporation with CuS was assisted by PXRD, FESEM, FEG-TEM, XPS, UV-vis and PL data. The importance of charge transport kinetics and higher charge carrier mobility of the photocatalysts for RhB decomposition was reported. It was seen that in the presence of visible light, the T-CuS exhibited higher photocatalytic activity than the bare CuS. The higher mobility of the composites helped the photo-induced charges to quickly transfer between the active site and the target molecules in the course of the degradation process. Strong interfacial contact, higher absorption of visible light and reduced recombination of e^-–h^+ pairs are the additional crucial key factors for enhancing the photocatalytic performance of the composites. Overall, addressing the challenge of visible light-induced photocatalysis, the superiority of the CNT composites over the as-synthesized bare CuS catalysts was demonstrated in this study. Finally, our results shed light on the design of carbon-based semiconductor (T-CuS) composites and established them as promising photocatalysts for various potential applications in wastewater treatment.

Conflicts of interest

There are no conflicts to declare.

Acknowledgements

The authors would like to give special thanks to the University Grants Commission (UGC) for providing the NET-SRF fellowship programme.

References

1 R. Al-Tohamy, S. S. Ali, F. Li, K. M. Okasha, Y. A. G. Mahmoud, T. Elsamahy, H. Jiao, Y. Fu and J. Sun, *Ecotoxicol. Environ. Saf.*, 2022, 231.
2 V. Selvaraj, T. Swarna Karthika, C. Mansiya and M. Alagar, *J. Mol. Struct.*, 2021, **1224**, 129195.
3 M. A. Al-Nuaim, A. A. Alwasiti and Z. Y. Shnain, *Chem. Pap.*, 2022, **77**, 677–701.
4 S.-Y. Wang, J.-Y. Ma, Z.-J. Li, H. Q. Su, N. R. Alkurd, W.-L. Zhou, L. Wang, B. Du, Y.-L. Tang, D.-Y. Ao, S.-C. Zhang, Q. K. Yu and X.-T. Zu, *J. Hazard. Mater.*, 2015, **285**, 368–374.
5 O. Elbanna, M. Zhu, M. Fujitsuka and T. Majima, *ACS Catal.*, 2019, **9**, 3618–3626.
6 T. Aarthi and G. Madras, *Ind. Eng. Chem. Res.*, 2007, **46**, 7–14.
7 F. Ghribi, A. Alyamani, Z. ben Ayadi, K. Djessas and L. el Mir, in *Energy Procedia*, Elsevier Ltd, 2015, vol. 84, pp. 197–203.
8 T. Kajana, A. Pirashanthan, D. Velauthapillai, A. Yuvapragasam, S. Yohi, P. Ravirajan and M. Senthilnanthanan, *RSC Adv.*, 2022, **12**, 18041–18062.
9 D. Wang, M. Sun, G. Feng and C. Song, *J. Mater. Eng. Perform.*, 2019, **28**, 6649–6655.
10 N. Ul Ain, J. A. Nasir, Z. Khan, I. S. Butler and Z. Rehman, *RSC Adv.*, 2022, **12**, 7550–7567.
11 M. Baláž, E. Dutková, Z. Bujňáková, E. Tóthová, N. G. Kostova, Y. Karakirova, J. Briančin and M. Kaňuchová, *J. Alloys Compd.*, 2018, **746**, 576–582.
12 X. Meng, L. Shi, L. Cui, L. Yao and Y. Zhang, *Mater. Res. Bull.*, 2021, **135**, 111156.
13 J. C. Ortiz-Herrera, H. Cruz-Martínez, O. Solorza-Feria and D. I. Medina, *Int. J. Hydrogen Energy*, 2022, **47**, 30213–30224.
14 Y. Huang, R. Li, D. Chen, X. Hu, P. Chen, Z. Chen and D. Li, *Catalysts*, 2018, **8**, 151.
15 R. Sarkar, M. Kar, M. Habib, G. Zhou, T. Frauenheim, P. Sarkar, S. Pal and O. v. Prezhdo, *J. Am. Chem. Soc.*, 2021, **143**, 6649–6656.
16 X. He, X. Xu, G. Bo and Y. Yan, *RSC Adv.*, 2020, **10**, 2180–2190.
17 Y.-L. Chen, Z.-A. Hu, Y.-Q. Chang, H.-W. Wang, Z.-Y. Zhang, Y.-Y. Yang and H.-Y. Wu, *J. Phys. Chem. C*, 2011, **115**, 2563–2571.
18 M. Varga, T. Izak, V. Vretenar, H. Kozak, J. Holovsky, A. Artemenko, M. Hulman, V. Skakalova, D. S. Lee and A. Kromka, *Carbon*, 2017, **111**, 54–61.
19 M. Chandra, K. Bhunia and D. Pradhan, *Inorg. Chem.*, 2018, **57**, 4524–4533.
20 Y. Yan, H. Yang, Z. Yi, T. Xian, R. Li and X. Wang, *Desalin. Water Treat.*, 2019, **170**, 349–360.
21 J. Tauc, R. Grigorovici and A. Vancu, *Phys. Status Solidi B*, 1966, **15**, 627–637.
22 Z. Huang, L. Wang, H. Wu, H. Hu, H. Lin, L. Qin and Q. Li, *J. Alloys Compd.*, 2022, **896**, 163045.
23 M. Tanveer, C. Cao, I. Aslam, Z. Ali, F. Idrees, M. Tahir, W. S. Khan, F. K. Butt and A. Mahmood, *RSC Adv.*, 2014, **4**, 63447–63456.
24 P. Borthakur, P. K. Boruah, G. Darabdhara, P. Sengupta, M. R. Das, A. I. Boronin, L. S. Kibis, M. N. Kozlova and V. E. Fedorov, *J. Environ. Chem. Eng.*, 2016, **4**, 4600–4611.
25 Z. Chen, S. Berciaud, C. Nuckolls, T. F. Heinz and L. E. Brus, *ACS Nano*, 2010, **4**, 2964–2968.
26 S. Iqbal, A. Bahadur, A. Saeed, K. Zhou, M. Shoaib and M. Waqas, *J. Colloid Interface Sci.*, 2017, **502**, 16–23.
27 P. Madhusudan, J. Zhang, B. Cheng and G. Liu, *CrystEngComm*, 2013, **15**, 231–240.
28 Y. Quan, M. Zhang, G. Wang, L. Lu, Z. Wang, H. Xu, S. Liu and Q. Min, *New J. Chem.*, 2019, **43**, 10906–10914.
29 Q. Yang, X. Guo, W. Wang, Y. Zhang, S. Xu, D. H. Lien and Z. L. Wang, *ACS Nano*, 2010, **4**, 6285–6291.
30 T. Dürkop, S. A. Getty, E. Cobas and M. S. Fuhrer, *Nano Lett.*, 2004, **4**, 35–39.
31 İ. Taşçıoğlu, U. Aydemir and Ş. Altındal, *J. Appl. Phys.*, 2010, **108**, 064506.
32 I. Ullah, M. Shah, M. Khan and F. Wahab, *J. Electron. Mater.*, 2016, **45**, 1175–1183.

33 M. Soylu and B. Abay, *Phys. E*, 2010, **43**, 534–538.
34 S. Sil, A. Dey, J. Datta, M. Das, R. Jana, S. Halder, J. Dhar, D. Sanyal and P. P. Ray, *Mater. Res. Bull.*, 2018, **106**, 337–345.
35 M. Das, J. Datta, A. Dey, R. Jana, A. Layek, S. Middya and P. P. Ray, *RSC Adv.*, 2015, **5**, 101582–101592.
36 D. Das, M. Das, S. Sil, P. Sahu and P. P. Ray, *ACS Omega*, 2022, **7**, 26483–26494.
37 S. Khanchandani, S. Kundu, A. Patra and A. K. Ganguli, *J. Phys. Chem. C*, 2013, **117**, 5558–5567.
38 J.-M. Herrmann, *Catal. Today*, 1999, **53**, 115–129.
39 Y. Ye, H. Yang, H. Zhang and J. Jiang, *Environ. Technol.*, 2020, **41**, 1486–1503.
40 S. Rawalekar, S. Kaniyankandy, S. Verma and H. N. Ghosh, *J. Phys. Chem. C*, 2011, **115**, 12335–12342.
41 D. K. Padhi and K. Parida, *J. Mater. Chem. A*, 2014, **2**, 10300–10312.
42 E. Alimohammadi, V. Mahdikhah and S. Sheibani, *Appl. Surf. Sci.*, 2022, **598**, 153816.
43 L. Huang, F. Peng, H. Yu and H. Wang, *Solid State Sci.*, 2009, **11**, 129–138.
44 M. Wang, L. Sun, Z. Lin, J. Cai, K. Xie and C. Lin, *Energy Environ. Sci.*, 2013, **6**, 1211.
45 Y. Du, Z. Niu, T. Yan, K. Zhu, Y. Yu and Z. Jing, *Front. Mater. Sci.*, 2021, **15**, 241–252.
46 Z. Zhang, S. Zhai, M. Wang, H. Ji, L. He, C. Ye, C. Wang, S. Fang and H. Zhang, *J. Alloys Compd.*, 2016, **659**, 101–111.